JOURNAL OF PROPULSION AND POWER
Vol. 25, No. 5, September–October 2009

Study of Restricted Shock Separation Phenomena in a Thrust Optimized Parabolic Nozzle

S. B. Verma* and O. Haidn†
DLR, German Aerospace Center, D-74239 Lampoldshausen, Germany

DOI: 10.2514/1.42351

An experimental investigation has been carried out on a subscale thrust optimized parabolic nozzle (area ratio of 30) to study the flow characteristics prevalent during a partially formed restricted shock separation and a fully formed restricted shock separation condition, each of which are observed to be discrete in nature. Whereas the wall pressure signal near the nozzle exit randomly alternates between its value in the backflow region and that above ambient (i.e., flow randomly alternates between a free shock separation and restricted shock separation transition condition and vice versa) as a function of time for a partially formed restricted shock separation condition, the wall pressure in a fully formed restricted shock separation condition fluctuates in values above ambient in the region of flow reattachment. Further, the transient conditions of free shock separation to partially formed restricted shock separation and end-effect regime are studied in detail. The preceding transitions and retransitions suggest a variation in the relative axial positions of normal and separation shocks that favors a fully formed restricted shock separation to occur during shutdown. A second separation bubble is also observed in the restricted shock separation condition, the formation and opening of which is seen to contribute toward side-load peaks. Results also indicate that the separation shock translates back and forth (flapping motion) and experiences spanwise perturbations (rippling motion). The results are based on simultaneously acquired real-time wall pressure measurements, surface oil visualization technique, high-speed schlieren images, and signals from strain gauges installed on the nozzle bending tube.

Nomenclature

C_O	=	overexpansion shock
C_R	=	reflected shock
C_N	=	normal shock
f	=	fluctuation frequency, Hz
$G(f)$	=	power spectral density, bar^2/Hz
P_a	=	ambient pressure, bar
P_{inc}	=	wall pressure at the point of incipient separation, bar
P_{pl}	=	plateau pressure after separation, bar
P_w	=	local wall pressure, bar
P_0	=	pressure in the stagnation chamber, bar
r_t	=	radius of nozzle throat, mm
T	=	triple point
t	=	time at a particular sequence of events, s
V	=	voltage signal from the strain gauges installed in the bending tube, mV
X	=	coordinate along the nozzle axis, mm
X_{exit}	=	X location at nozzle exit, mm
X_{inc}	=	point of incipient separation (measured up to the first rise in wall pressure), mm
X_{sep}	=	point of physical flow separation (measured up to the upstream extent of oil-pigment accumulation as seen from surface oil flow tests), mm
$X_{\text{sep}_{\text{bub}}}$	=	length of separation bubble (measured from the upstream to downstream extent of oil-pigment accumulation as seen from surface oil flow tests), mm
θ_w	=	nozzle wall angle, deg
$\theta_{w_{\text{exit}}}$	=	nozzle exit wall angle, degrees
σ	=	rms fluctuation of the local wall pressure
ϕ	=	angle measured along the nozzle circumference, deg

Presented as Paper 1431 at the 44th Aerospace Sciences Meeting and Exhibit 2006, Reno, NV, 9–12 January 2006; received 24 November 2008; revision received 30 April 2009; accepted for publication 13 July 2009.

*Research Scientist, Experimental Aerodynamics Division, National Aerospace Laboratories, Council of Scientific and Industrial Research, Bangalore 560 017, India; sbverma@ead.cmmacs.ernet.in.

†Head of Technology and Vice Director, Institute of Space Propulsion; oskar.haidn@dlr.de. Associate Fellow AIAA.

Introduction

HIGH expansion nozzles such as the thrust optimized parabolic (TOP) and the compressed truncated perfect contour (CTP) are used in the main engines of present day launch vehicles to increase the vacuum performance. However, during sea-level ignition, such as the transient startup condition, the flow tends to separate inside such nozzles. The strong unsteadiness associated with the separation shock in combination with any flow asymmetry can generate dangerous side loads. The shock structure in the exhaust of such nozzles can further dictate the side-load activity considerably. For example, the exhausts from the TOP and CTP nozzles feature an internal shock that originates slightly downstream of the point (at the beginning of the divergent section) where the wall contour undergoes a transition in its curvature from circular arc (which forms the throat section) to parabolic contour. At this transition point, the wall contour and wall slope are both continuous, whereas the wall curvature is discontinuous [1]. Further, the parabola is not adapted to the expansion waves coming from the throat (unlike the ideal nozzle design). As a result, compression waves are induced by the parabola leading to formation of an internal shock [2–7]. The exhaust flow structure from such parabolic nozzles gives an appearance of a cap and hence is popularly known as a cap-shock pattern [6–8]. This shock pattern results from an interaction of the overexpansion or the separation shock (coming from the nozzle wall) and an inverse Mach reflection of the internal shock at the nozzle centerline (see Fig. 1). Such cap-shock patterns have also been observed in the hot-firing tests of the space shuttle main engine, the Vulcain 1 and 2 engines [6,9], and the Japanese LE-7A engine [10,11] and are known to be associated with considerable side-load activity [9,10,12].

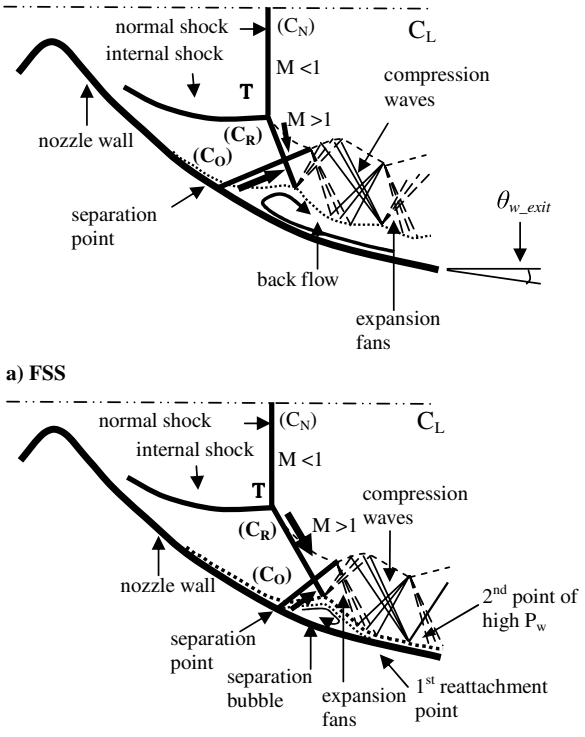

Fig. 1 Schematic of a) free shock separation and b) restricted shock separation condition inside a thrust optimized parabolic nozzle.

Flow separation and the associated side loads in rocket nozzles have been the subject of research, both experimentally and numerically. Initially, Nave and Coffey [12], during the Apollo developmental program in 1970, observed in their cold-flow subscale nozzle tests of the J-2S engine that flow reattachment downstream of separation can occur, leading to dangerous lateral forces. Recently [2–9,13–17], it has been observed that the side loads in a TOP nozzle are associated with conditions of flow transition such as free shock separation (FSS) to restricted shock separation (RSS) and vice versa. The key driver to such flow transitions was reported [6] to be the momentum imbalance of flow passing through the overexpansion C_O and reflected C_R shocks, Fig. 1, which in turn is initiated by the nonuniform rates of normal shock movement relative to the separation point movement at different nozzle pressure ratios (NPRs). Recently, Stark et al. [14] demonstrated the presence of a recirculation bubble in the jet of the nozzle, downstream of the cap-shock pattern. Kwan and Stark [15] further showed that the mutual interaction of the shock pattern and this recirculation region behind the cap shock can cause a short, asymmetric reattachment of the flow on the nozzle wall, leading to a quasi-restricted shock separation (qRSS) condition that induces lateral forces at low NPRs. Verma and Ciezki [18] demonstrated that the flow unsteadiness accompanying the downstream jump in separation front (during startup sequence) leads to a strong side-load condition. More recently, Verma et al. [19,20] showed that the unsteadiness linked with different flow separation modes and transitions can be related with peaks in side-load signal at various flow conditions. Infrared thermometry studies by Gross et al. [21] and Stark et al. [14] for the RSS condition showed an increase in local wall temperature in the region of the separation and reattachment line. Further, the concave curvature of the reattaching boundary layer was seen to result in streamwise counter-rotating vortices. The surface trail left by these vortices (in the form of a striation pattern) was observed for the first time using a conventional surface oil-pigment visualization technique [22], but only when the RSS condition occurred during shutdown sequence. All of the preceding results added vital information that led to the knowledge of flow behavior prevalent inside rocket nozzles. The present paper is a continuing effort to further understand these complex flows conditions. A detailed overview of the studies on rocket nozzles can also be found in [23,24].

The present paper reports the results of an experimental investigation conducted in a subscale cold gas test facility on a thrust optimized parabolic rocket nozzle. The main emphasis is to primarily investigate the flowfield characteristics prevalent during partially formed restricted shock separation (pRSS) and end-effect regime in detail during startup ($\delta P_0/\delta t > 0$) and fully formed restricted shock separation condition during shutdown ($\delta P_0/\delta t < 0$). The test model used is the same TOP nozzle previously used by Frey and Hagemann [3,6], Hagemann et al. [4], Gross et al. [21], and Stark et al. [14]. Streamwise wall pressure measurement data are acquired along the nozzle contour using fast piezoresistive pressure sensors, whereas a surface oil-pigment visualization method is employed to investigate the subtle changes in surface flow behavior in response to varying nozzle operating conditions.

Experimental Setup and Procedure

Test Facility

Tests were carried out in the subscale cold gas test facility [7,8] enhanced with an additional horizontal test bench, as shown in Fig. 2a (see [15] for more details), and not in the high-altitude simulation chamber which limits visibility during test campaigns with surface oil flow, infrared thermometry, etc. This facility uses dry nitrogen at ambient temperature as the test gas due to its advantage over compressed air, that is, the absence of humidity and other impurities that can otherwise cause condensation of flow during operation. The nozzle pressure ratio was adjusted by varying the nozzle feeding pressure P_0 and, under present test limitations with the nozzle blowing into atmospheric pressure, a maximum pressure ratio up to 60 can be achieved. The throat diameter of the subscale thrust optimized parabolic nozzle used for the experimental investigation was 20 mm, yielding maximum mass flows in the range of $m = 4.2$ kg/s. A TOP nozzle of moderate area ratio (30) is used. The TOP nozzle was designed at DLR using the skewed parabolic geometry approximation proposed by Rao [25] from inflection point to the nozzle exit. More details regarding the nozzle's design can be found in [8].

Wall Pressure Sensors and Data Acquisition

Wall pressures both upstream and downstream of the throat are measured using fast piezoresistive pressure sensors (Kulite

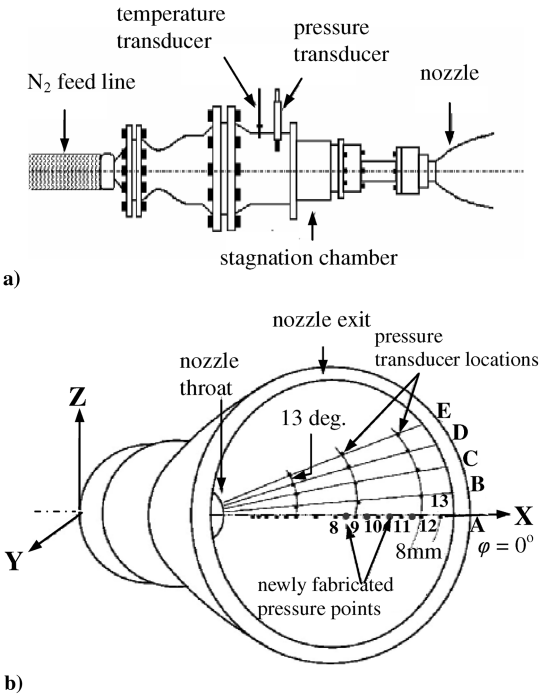

Fig. 2 Schematic of the a) nozzle test facility at DLR P6.2 and b) pressure sensor locations and the choice of axis.

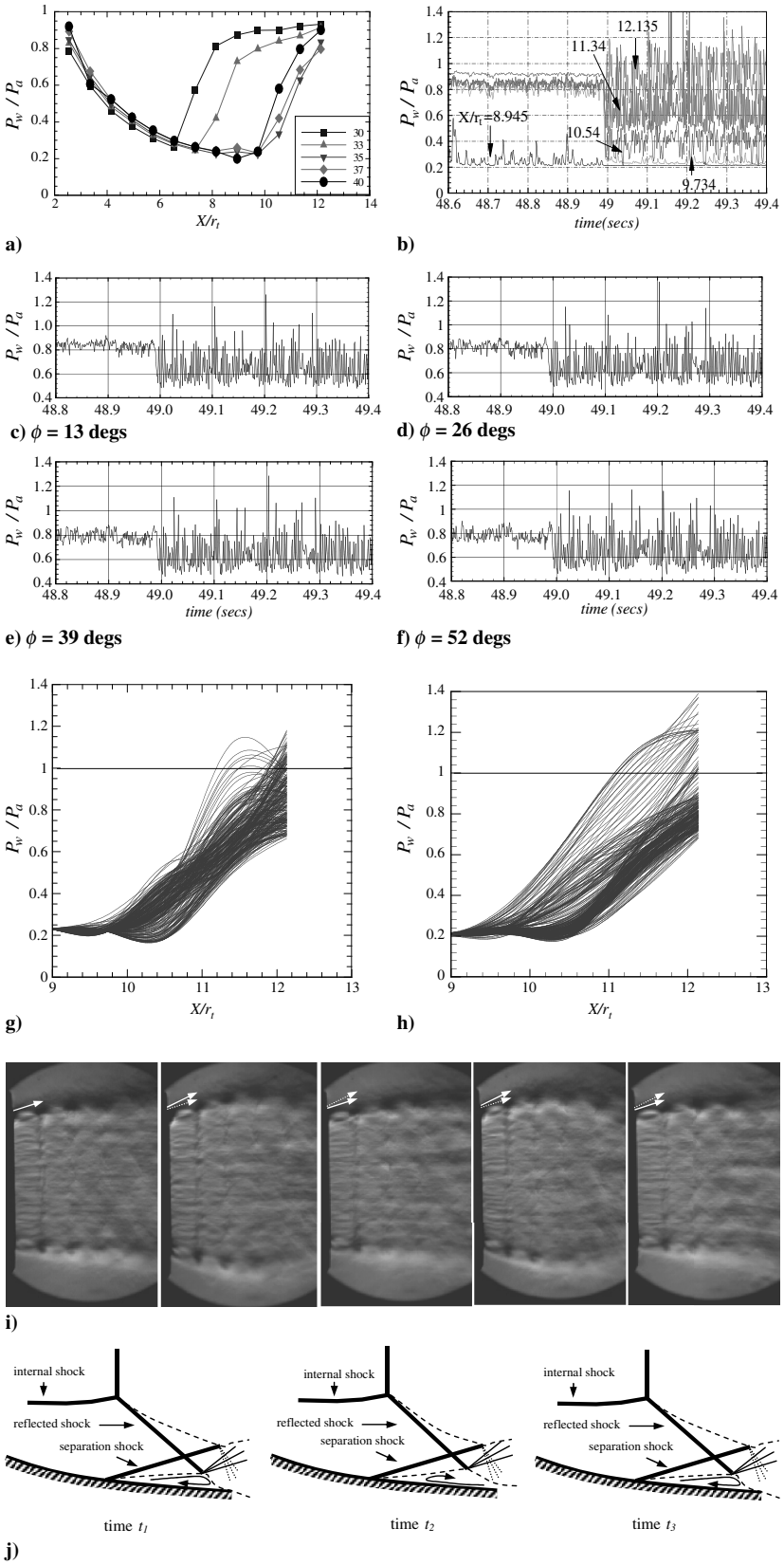

Fig. 3 Flow characteristics prevalent during pRSS condition: startup sequence.

Semiconductor, Inc., model XT-140M). These transducers have a pressure-sensitive area of 0.71 mm in diameter and an outer case diameter of 3.9 mm. According to the manufacturer's specifications, these transducers have a natural frequency of 50 kHz. They are capable of operating in the temperature range of -40 to $+85^{\circ}$C and in the range of 0–100% relative humidity. The accuracy, according to manufacturer's specification is within 0.5% in the operating pressure range of 0–1 bar. The sensitivity of the transducers is typically 97.206 mV/bar. All the transducers were calibrated statically against atmospheric pressure. Four such pressure sensors are placed in the stagnation chamber and 13 along a single axial line in the supersonic section of the nozzle (with a pitch of 8 mm, sampling frequency 1 kHz with low-pass filter cutoff frequency of 160 Hz). In addition to these, four more pressure points were fabricated recently,

one each midway between the pressure points 8–12 to capture flow details during RSS at various NPRs. Data for transducers at the 12th location (i.e., 12A, 12B, 12C, 12D, and 12E) are acquired at 10 kHz to study circumferential variations in pressure fluctuations. Figure 2b shows the choice of axis and the pressure transducer locations for the present tests. A data acquisition system is used which has the capacity of measuring 64 channels at 1 kHz and 16 at 50 kHz or 8 at 100 kHz.

Surface flow patterns were visualized using the classic oil-pigment mixture (using vacuum pump oil, titanium dioxide, and oleic acid). Online recording of visualization tests was done with a camera looking up into the nozzle, which was later digitized to extract vital flow information such as small movements of the physical separation location especially during the pRSS condition and end-effect regime.

Results and Discussions

Mean Pressure Distributions

As the nozzle pressure ratio is increased, the shock structure from the TOP nozzle preserves itself and moves downstream, as sketched in Fig. 1a. When the separation point is pushed close to the nozzle exit, the difference in local nozzle wall angle θ_w at X_{sep} and nozzle exit wall angle $\theta_{w_{\text{exit}}}$ at X_{exit} becomes very small, thereby reducing the gap between the nozzle wall and the lower limit of mixing layer. The reduction in radial size of the recirculation zone in the backflow region has the potential to initiate a partial or full reattachment of flow downstream of separation at the point where the expansion fan (formed as a result of the overexpansion or separation shock being reflected from the inner shear layer) hits the outer shear layer (Fig. 1a). This may be strongly influenced by the type of nozzle contour (which also dictates the shock structure) and, more important, the test environment into which the nozzle exhausts, for example, open atmosphere or in a high-altitude chamber using either self-evacuation mode or ejector effect.

Figure 3a shows the streamwise mean wall pressure distributions for a certain range of nozzle pressure ratios during the startup sequence. Each of these is obtained by holding the stagnation pressure constant for approximately 15 s. Here, the wall pressure P_w is nondimensionalized by the ambient pressure P_a, and the nozzle axial distance X is nondimensionalized by the nozzle throat radius r_t. It can be seen that, as the flow accelerates, it expands until at some downstream location it experiences a sudden jump in wall pressure indicating an incipient separation point. Thereafter, a gradual pressure adaptation to the ambient pressure occurs over the remaining length of the nozzle. The pressure in this region was generally observed to remain in the range of 0.8–0.95. This region is known as the backflow region wherein the pressure drop occurs due to acceleration of ambient air caused by the pumping action of the separated mixing layer. Increase in the NPR pushes the incipient separation point downstream accompanied by a reduction in length of the backflow region. Between NPR = 33 and 35, a flow transition is observed during which the incipient separation point jumps downstream significantly from its location at $X/r_t = 7.35$ to 9.735. For NPR = 35 and 37, it is important to note that the pressure distribution shows a backflow region that seems to be partially closed (discussed later) and indicated by the lower pressure adaptation at these NPRs. At NPR = 40, the separation location is slightly pushed upstream and the wall pressure distribution once again shows a better pressure adaptation after separation to almost 0.9. This indicates a change in flow condition wherein the partially closed backflow region completely opens once again allowing the ambient air to accelerate into the nozzle.

Figure 3b shows the time history of streamwise wall pressure signals from pressure sensors that experience the FSS → pRSS transition as NPR = 35 is reached (Fig. 3a) during startup. Careful evaluation of the raw pressure signals shows that this transition lasts for about 10 ms. This NPR of 35 is then held constant for 15 s, during which the wall pressure signal from the 12th and 13th ($X/r_t = 11.34$, 12.135, and closest to nozzle exit) transducer locations is seen to fluctuate between its value in the backflow region and that above ambient as a function of time. The time history of wall pressures from circumferentially placed transducers at the 12th location (and acquired at 10 kHz), Figs. 3c–3f, for the same test run also shows similar characteristics as observed in Fig. 3b. Figures 3g and 3h show the fluctuations of instantaneous wall pressure distributions for the pRSS condition during startup (250 randomly selected samples) for NPR = 35 and 37, respectively, for the test cases shown in Fig. 3a. It is clearly seen that the flow randomly alternates between FSS to RSS transition and vice versa as a function of time. The number of instants that show the FSS condition are significantly more than that for the RSS condition, and so the flow does not fully reattach exhibiting the pRSS condition. Figure 3i shows high-speed schlieren (2 kHz) images of nozzle exhaust flow for NPR = 37 during startup. The sequence of events shows pRSS flow condition with alternating FSS to RSS transition and vice versa (each event is separated by a time interval of 0.5 ms). Here, each sequence of events is separated by 0.5 ms. The nozzle exhaust flow pattern can be seen to fluctuate significantly in its lateral extent (white bold arrows represent the exhaust direction in the present event, whereas the dotted arrow represents exhaust direction from the previous event) in each sequence and does not, at any time, show a steady full-flowing nozzle as seen later for a fully formed RSS condition, as shown later. Because of such a flow condition, the 12th and 13th transducer locations show the wall pressure fluctuating between its value in the backflow region and that above ambient as a function of time. Figure 3j shows a schematic representation of the pRSS phenomena for three successive time instants depicting the sequence of events during the randomly alternating FSS to RSS transition and vice versa as developed from schlieren images and alternating wall pressures. These

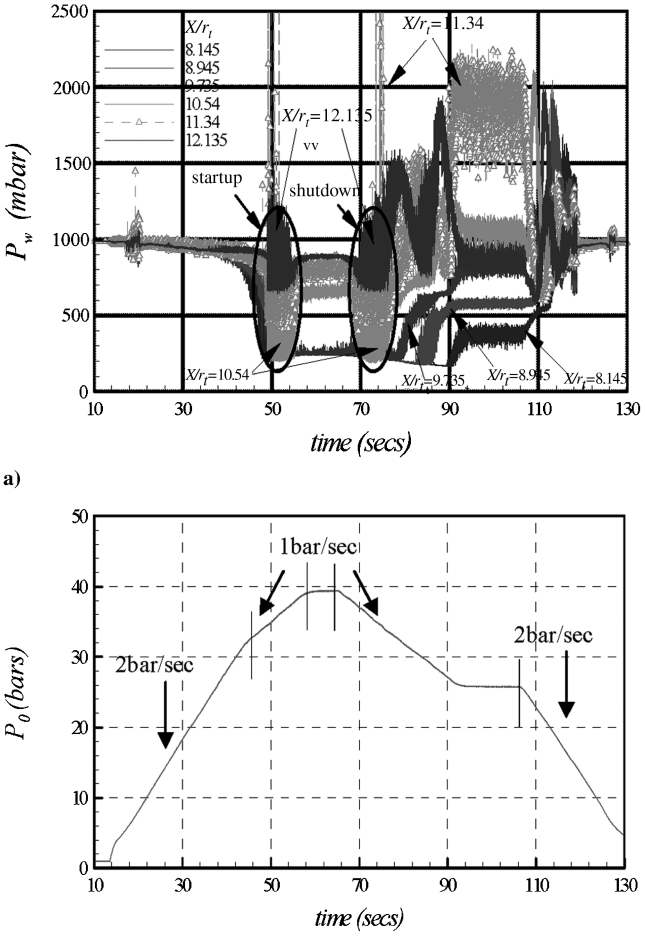

Fig. 4 Time history of a) wall pressure signals at $\phi = 0$ deg, and b) the corresponding stagnation pressure variation. The numbers in the legend show the streamwise pressure transducer positions (8–13) on the nozzle wall.

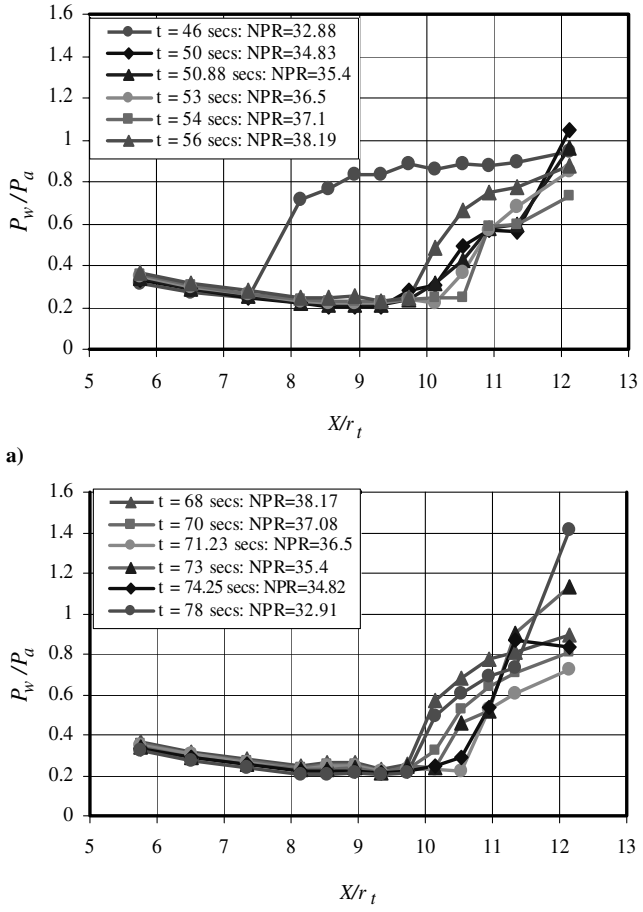

Fig. 5 Wall pressure distribution at different time instants and selected randomly for a) NPR = 32–40 for startup sequence, and b) NPR = 40–32 for shutdown sequence.

fluctuating wall pressure and exhaust flow characteristics are typical to a partially closed backflow or partially formed restricted shock separation and will be referred hereafter as the pRSS condition. This flow condition therefore occurs when the separation point approaches closer to the nozzle exit and the flow is unable to reattach fully on the nozzle walls. An immediate and a very distinct consequence of the pRSS condition is that, for the entire time duration it lasts, no closed separation bubble (region of pigment accumulation) and reattachment region are formed (with repeated tests) on the nozzle surface as is observed for a fully formed RSS condition (discussed later). These typical flow features prevalent during the pRSS condition significantly differentiates itself from a fully formed RSS condition.

Earlier tests made by Hagemann et al. [4], Frey and Hagemann [6], and Frey et al. [8] with the same subscale TOP nozzle observed a transition from FSS to fully formed restricted shock separation during the startup phase at NPR = 33.3 and 33.7 [7]. However, in the present tests, the pRSS condition is always observed (with repeated tests) during startup sequence between NPR = 35 and 37, during which the flow randomly alternates between an FSS and RSS transition and vice versa as a function of time. It may, however, be pointed out here that Frey and Hagemann [6] and Frey et al. [8] carried out their tests in the high-altitude simulation chamber (HASC) in P6.2 (with HASC in self-evacuation mode and using a supersonic diffuser), whereas the results presented in this paper are from tests made in a separate horizontal test bench, especially developed in 2001 to have better optical access when looking up into the nozzle. This test bench is open to the atmosphere and is therefore free from any interference effects caused by the possible interaction between the altitude chamber, nozzle, and diffuser in the HASC. Therefore, the flow characteristics during the pRSS condition need to be carefully studied and discussed in detail. Another flow regime that needs scrutiny is the end-effect regime first qualified by Nave and Coffey [12]. This is a flow condition wherein the point of reattachment (in our case, the point of partial reattachment after transition) reaches the nozzle lip and the partially closed recirculation bubble opens to ambience.

End-Effect and pRSS Flow Conditions

Figures 4a and 4b show the time history of axially located wall pressure transducers and the corresponding stagnation pressure, respectively, for a particular test campaign. Here, P_0 is initially increased at 2 bar/s up to NPR = 32 and thereafter slowed down deliberately to 1 bar/s, primarily to study in detail the transient flow conditions during the FSS → pRSS transition and the end-effect regime. Similarly, during shutdown, the stagnation pressure is again decreased at 1 bar/s until the NPR of interest (with fully formed RSS condition) is reached, which is then held constant for 15 s. The circumferential angle is defined as ϕ and is taken as zero for axially located pressure transducers (as a reference). Several such

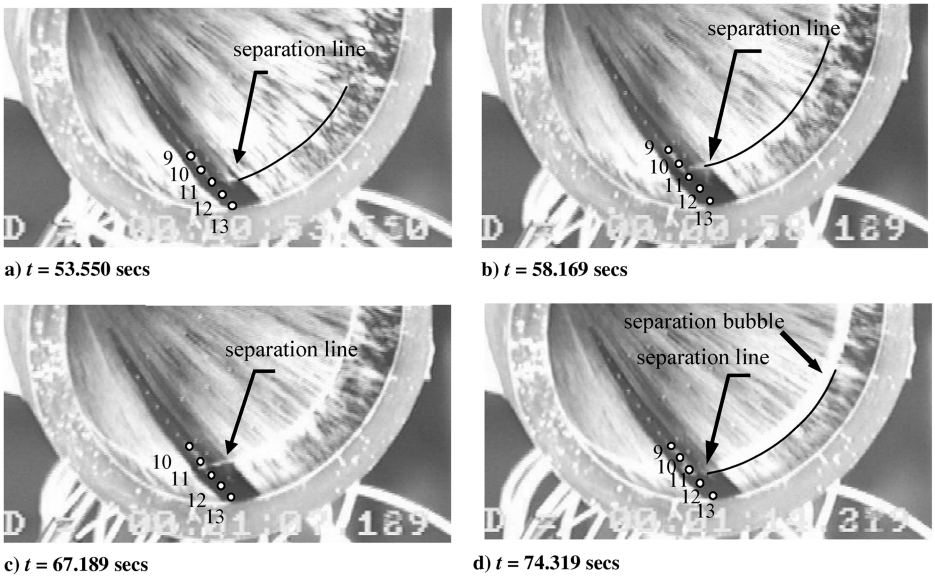

Fig. 6 Surface oil visualization pictures during the test run showing separation movement during a) NPR = 36.8 to b) NPR = 38.2 pRSS → end-effect condition (startup), and during shutdown for c) NPR = 37 and d) NPR = 34 end effect → RSS, respectively.

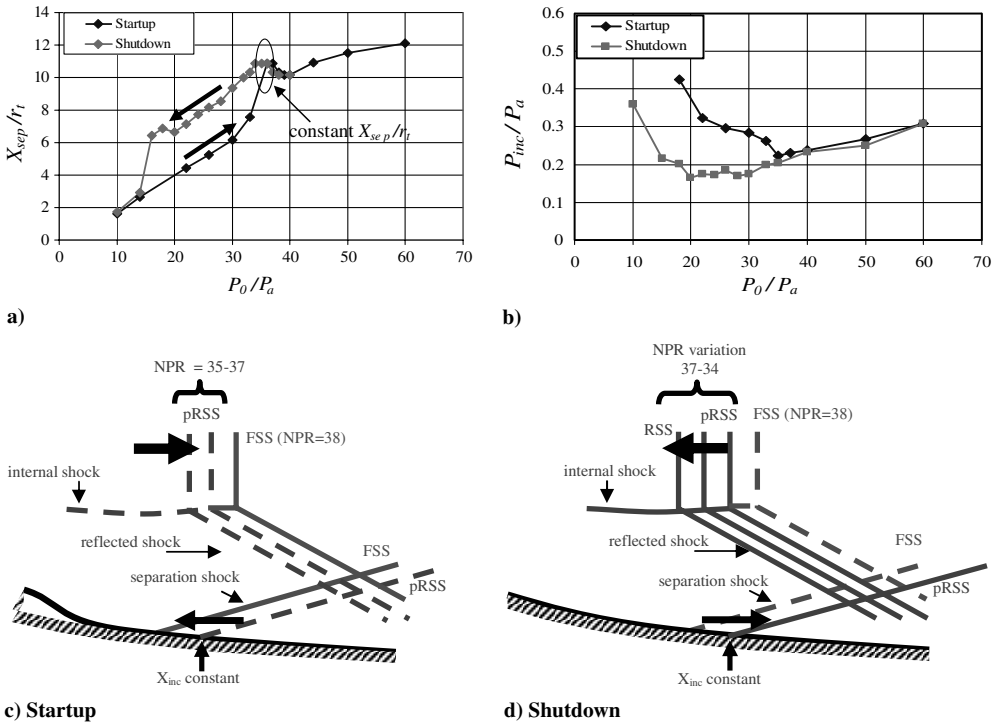

Fig. 7 Plots showing: a) variation of physical separation point (X_{sep}/r_t) movement during startup and shutdown, b) comparison of wall pressure at the incipient separation point location during startup and shutdown sequence, and c–d) schematic illustration of the possible phenomena during startup and shutdown.

independent tests were made for different NPRs of interest during shutdown to study the flow phenomena during fully formed RSS.

Two main areas of interest are marked on the plot by ellipses which depict the FSS → pRSS transition and the end-effect flow condition (pRSS → FSS) during startup ($\delta P_0/\delta t > 0$) and the FSS → pRSS and pRSS → RSS transition during the shutdown ($\delta P_0/\delta t < 0$) sequence, respectively. Thereafter, for $t > 76$ s and NPR ≤ 33, the wall pressures (from a few transducer locations) show values significantly above ambient pressure. This indicates the prevalence of a fully formed RSS condition during shutdown which is very different from the pRSS condition. Instantaneous but randomly selected streamwise wall pressure distributions during the startup flow transitions are shown in Figs. 5a and 5b and by the simultaneous oil pictures in Figs. 6a–6d, respectively. Wall pressure distributions for a startup case, Fig. 5a, show a significant downstream jump in the separation front in going from NPR = 32.88 to 34.83, which has been identified by Verma and Ciezki [18] to be responsible for the highest peak in strain-gauge signal during startup. The end of this transition occurs as NPR = 35 is reached. The flow at this NPR now depicts a partially formed restricted shock separation condition wherein the flow randomly alternates between FSS and RSS transition condition and vice versa as a function of time but never fully reattaches, as shown in Fig. 3b. The physical separation line at this point of time is seen, Fig. 6a for NPR = 35, approximately midway between the 11th and 12th pressure point but no line of reattachment can be seen. As the NPR is further increased, the separation point, as well as the point of partial reattachment, is pushed slightly downstream until at NPR = 38 where the location of partially reattached flow reaches the nozzle exit, causing the partially closed backflow region to open up. This causes the ambient air to rush in, pushing the X_{sep} upstream by almost 8–9 mm, as seen in Figs. 5a and 6b for NPR = 38.19. This transition contributes to the second strongest peak in the strain-gauge signal during startup (as shown later). This is known as the end-effect regime wherein the flow can no longer reattach (even partially) on the nozzle walls and a transition from pRSS → FSS occurs.

To facilitate visualization of separation line movement during these flow transitions, the following procedure was followed. Before the test run, a tape was put on the streamwise pressure transducer locations before spraying the oil pigment and then removed, leaving a clear band of streamwise region. During the test run, the oil accumulated at the physical point of separation tends to relocate itself along the nozzle circumference, forming a clear line (in response to subtle changes in NPR) in this region. It is difficult to detect this surface flow movement if this experimental procedure is not well planned. Ideally speaking, with the upstream jump in separation location due to end effect, the recirculation zone should partially or completely close once again as NPR is increased and the process repeats itself indefinitely. But, in reality, this does not happen and only the FSS condition is observed thereafter. It was further observed [22] that NPR = 37 is a critical value in initiating RSS during shutdown.

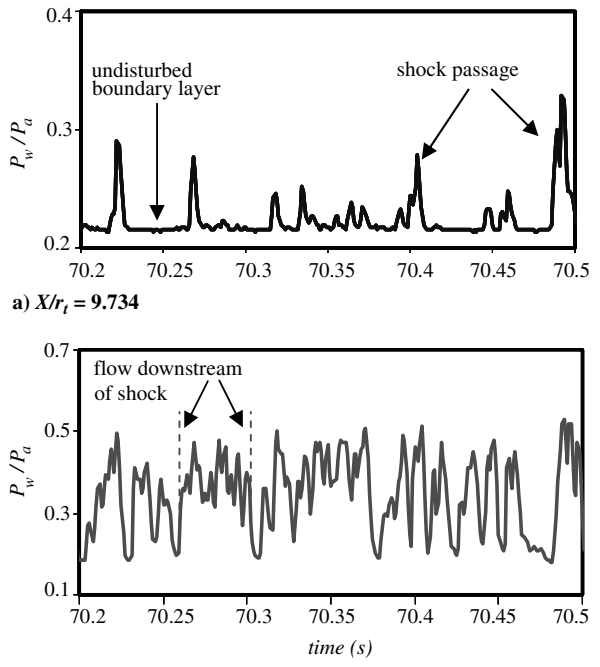

Fig. 8 Simultaneously sampled wall pressure signals in the intermittent region of separation, NPR = 35.

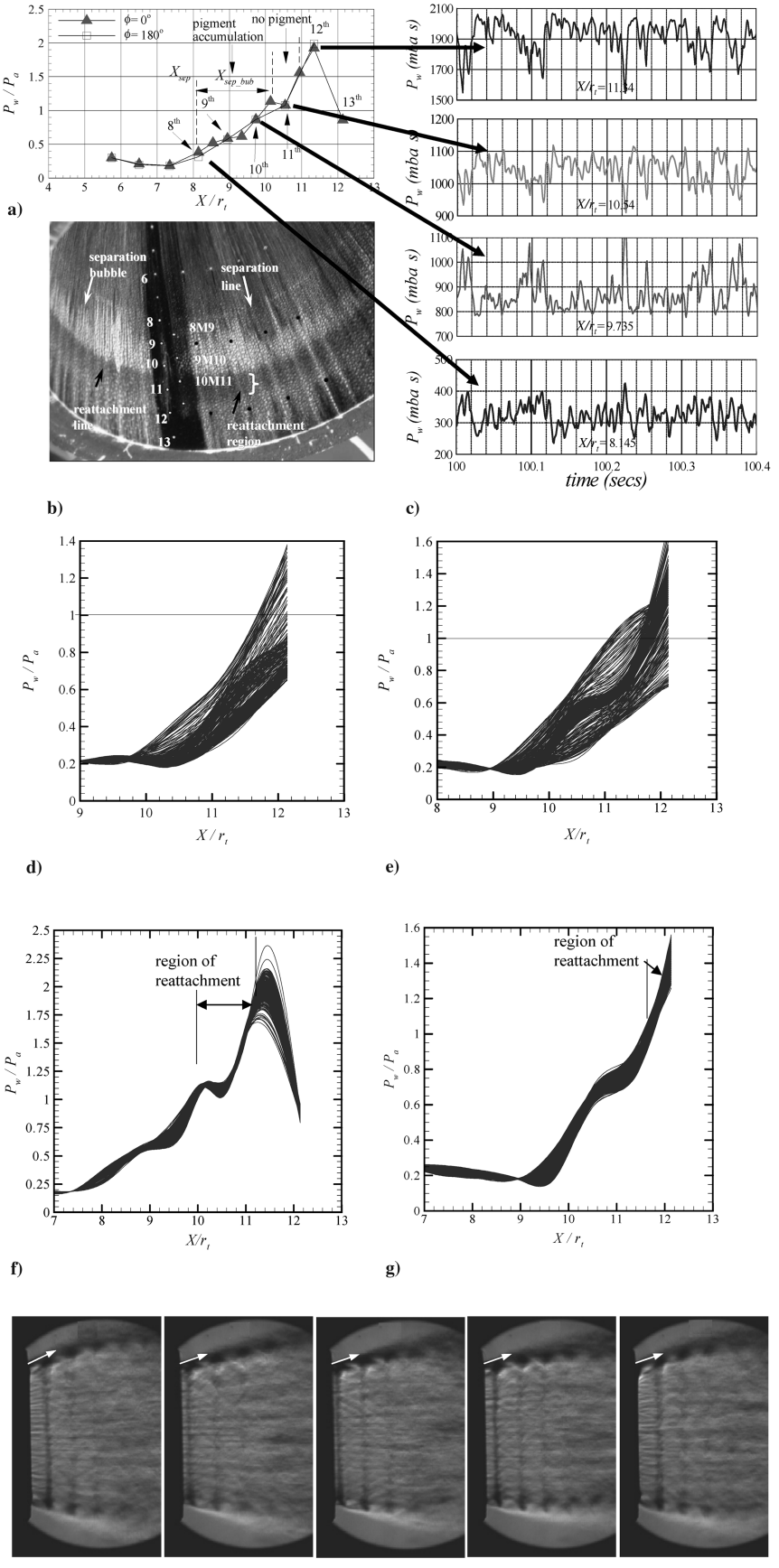

Fig. 9 Flow characteristics prevalent during fully formed RSS condition: shutdown sequence.

If this NPR value was not surpassed, RSS did not occur at all during shutdown. This is an important indication suggesting that a possible switch in the axial location of normal and separation shocks (i.e., normal shock moves downstream of separation shock location) occurs after the FSS → pRSS transition, which affects the flow transitions thereafter. Once these shocks switch positions, then, with increasing NPR, the flow passing the separation shock dominates the momentum balance and hence FSS alone is favored and the process is not repeatable. Frey and Hagemann [6] have also shown that the axial position of normal and separation shocks move at different rates at different power levels both for hot and cold gas, initiating different flow transitions. Fully formed RSS was, however, *not at all* observed during startup sequence in any of the test campaigns. Rather, each test repetition showed only a flow transition from FSS to pRSS that was accompanied by a significant downstream jump in separation front. *This was observed irrespective of the rate at which chamber pressure P_o was increased.*

The reverse, however, occurs during shutdown sequence, as can be seen in Figs. 5b, 6c, and 6d. As the NPR is decreased from 38 to 35, the separation front is initially pushed downstream indicating a FSS → pRSS transition (suggesting that the normal shock and overexpansion shock switch their respective axial positions once again), Figs. 6c and 6d. The wall pressure fluctuation during this flow condition is similar to that shown in Fig. 3g during startup except that it now shows more number of instants with RSS condition than FSS condition (as shown later). So this time, in going from NPR 35 to 33, the flow undergoes transition from pRSS to fully formed RSS unlike the case during startup where an FSS → pRSS transition occurs. It is also observed during shutdown that a fully formed RSS condition first occurs at NPR = 34 which can be confirmed from Fig. 6d where oil accumulation begins suggesting formation of a closed separation bubble. Earlier, Frey and Hagemann [1] also pointed out that a hysteresis exists in the flow separation process itself (in the form of separation pressure ratio $P_{\text{inc}}/P_{\text{pl}}$) which increases the potential of a fully formed RSS condition during shutdown.

Figures 7a and 7b show the variation of physical separation location X_{sep}/r_t (measured from surface oil study) and incipient separation pressure ratio (P_{inc}/P_a), respectively, as a function of nozzle pressure ratio. It is observed that, for NPR > 35, the trend in variation of X_{sep}/r_t and P_{inc}/P_a is similar for both startup and shutdown sequences, but the main deviation in these trends occurs for NPR < 35. For similar NPRs, P_{inc}/P_a is seen to be higher for the startup case relative to that for shutdown, Fig. 7b, whereas the corresponding X_{sep}/r_t values, Fig. 7a, are much less for startup relative to that for shutdown. Frey and Hagemann [3,6] suggested that the position of the normal shock is primarily dictated by the pressure ratio P_0/P_a which decides its strength to increase the pressure to ambient value. So for similar NPR during startup and shutdown, if the axial position of normal shock is considered the same, then a variation in the flow separation locations, as seen in Fig. 7a, can initiate a flow transition. A similar but a reverse trend can also be seen from Fig. 7a which shows that X_{sep}/r_t remains nearly constant between NPR 35 and 37 during startup and between NPR 36 and 34 during shutdown, respectively, and is explained schematically in Figs. 7c and 7d. During startup for NPR = 35 to 40, the incipient separation location X_{inc}/r_t also remains nearly constant, as seen in Fig. 3a. The observed constant X_{inc}/r_t location for NPR 35 and 40 might possibly be due to the 8 mm pitch for pressure sensor locations that may prevent detection of small changes in its movement. However, if a possible movement of X_{inc}/r_t position does exist, it is very small. So considering X_{inc}/r_t nearly constant for different normal shock positions (dictated by the NPR range) during startup and shutdown, different flow transitions can be expected once again (Figs. 7c and 7d). Therefore, during shutdown, as shown schematically in Fig. 7d, the flow passing the reflected shock dominates the momentum balance and hence a fully formed RSS is favored.

Fully Formed Restricted Shock Separation Condition

Kistler [26] and Dolling and Narlo [27] observed that a moving shock generates an intermittent wall pressure signal P_w whose level fluctuates between the range characteristic of the undisturbed turbulent boundary layer and that of disturbed flow downstream of the shock. Dolling and Narlo [27] further suggested that the instantaneous separation point and shock foot are essentially at the same location, whereas the physical separation line is the downstream boundary of a region of intermittent separation. Figure 8 shows the simultaneously sampled wall pressures for the present case in the vicinity of the separation location for NPR = 35 (startup). It can be observed that when the separation shock passes over the transducer it detects a rapid pressure rise, corresponding to sharp fronts in pressure signal. Within the region of shock motion, the wall pressure signal is intermittent, and around the mean position of the shock, low-frequency wall pressure fluctuations of large amplitude are present. Such knowledge of the flow dynamics is required to understand the flowfield mechanisms and to physically interpret the mean flow accurately.

Figure 9a shows the streamwise mean wall pressure distribution at NPR = 26 (and held constant for 15 s) during shutdown. A comparison with the surface oil picture, Fig. 9b, shows that the wall pressure rises gradually in the separation region, levels off somewhat in the fully separated zone, and then starts to rise again in the region of reattachment, eventually reaching its maximum value some distance downstream of the mean reattachment line. It can also be seen that the point of physical separation X_{sep} is at the eighth pressure point, that is, $X/r_t = 8.145$, whereas the flow reattachment occurs midway between the 10th and 11th points ($X/r_t = 10.14$) and the reattached boundary layer once again separates midway between the 11th and 12th pressure points. Two pressure plateau regions are formed, one indicating a separation bubble (where

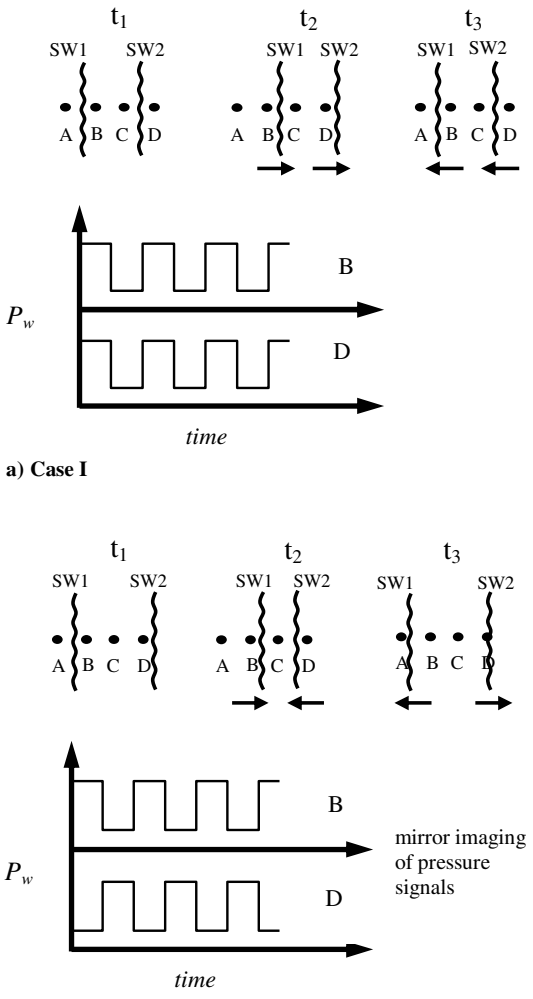

Fig. 10 Schematic of the prevalent shock motion as seen from the history of pressure signals from the transducers.

$P_w < P_a$) and the other a reattachment region (where $P_w > P_a$). Figure 9c shows the time history of wall pressure signals of interest [transducers 8 ($X/r_t = 8.145$), 10 ($X/r_t = 9.735$), 11 ($X/r_t = 10.54$), and 12 ($X/r_t = 11.34$)]. A careful examination of the signals indicate that transducers 10 and 11 show a mirror imaging of the pressure signal, whereas signals from transducers 8 and 10 and 11 and 12 change in concert with each other. At the end of the reattachment region (12th pressure point), the wall pressure further rises to twice the ambient pressure (due to the fan of compression waves being reflected from the nozzle wall as a single strong oblique shock, Fig. 1b) after which it decreases to near ambient value (13th point). This suggests that a small backflow region exists after the 12th pressure point.

Figures 9d and 9e show the fluctuations of the instantaneous wall pressure distributions of 250 samples for NPR = 36.4 and 34.3 showing prevalence of the pRSS condition during shutdown. The plot for NPR = 36.4 shows more instants of FSS than RSS, whereas, for NPR = 34.3, the plot shows more instants of RSS than FSS. As a result, RSS is preferred during shutdown for NPR $\leq$ 34 and the surface oil features begin to clearly form, as seen in Fig. 6d. Figures 9f and 9g show the fluctuations of the instantaneous wall pressure distributions of 250 samples for the test case of NPR = 26 shown in Fig. 9a and NPR = 32.65 during which a fully formed RSS condition exists. In both cases, it can be seen that, in the region of flow reattachment, the wall pressure remains above ambient at all times. Figure 9h shows the sequence of events for a fully formed RSS condition at NPR = 32.65 using a high-speed schlieren camera (2 kHz). Each sequence of events (left to right) is separated by a time interval of 0.5 ms. A full-flowing nozzle exhaust is clearly apparent from the schlieren images in all the time sequences (shown by a white arrow). Such a steadily full-flowing nozzle condition results in the formation of distinct surface flow features such as separation bubble, region of reattachment, etc., as seen in Fig. 9b. These flow features of a fully formed RSS are distinctly different from the pRSS condition, as discussed earlier. The RSS condition therefore needs to be broadly subdivided into a partially formed RSS (as the separation point approaches closer to nozzle exit and before the end effect finally occurs) and a fully formed RSS.

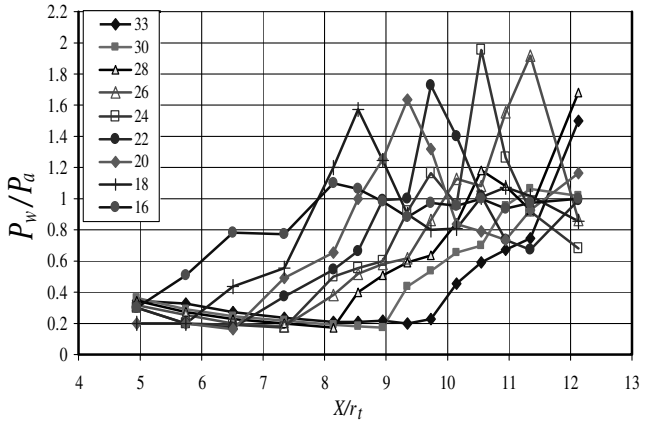

a)

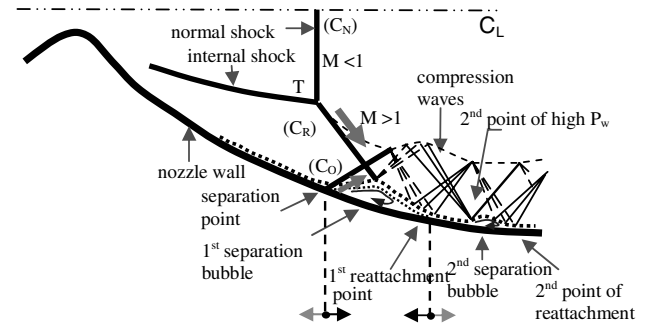

b)

Fig. 11 Mean flow prevalent during fully formed RSS condition: a) wall pressure distributions for RSS at various NPR during shutdown, and b) schematic sketch of RSS condition showing two separation bubbles and the prevalent shock motions.

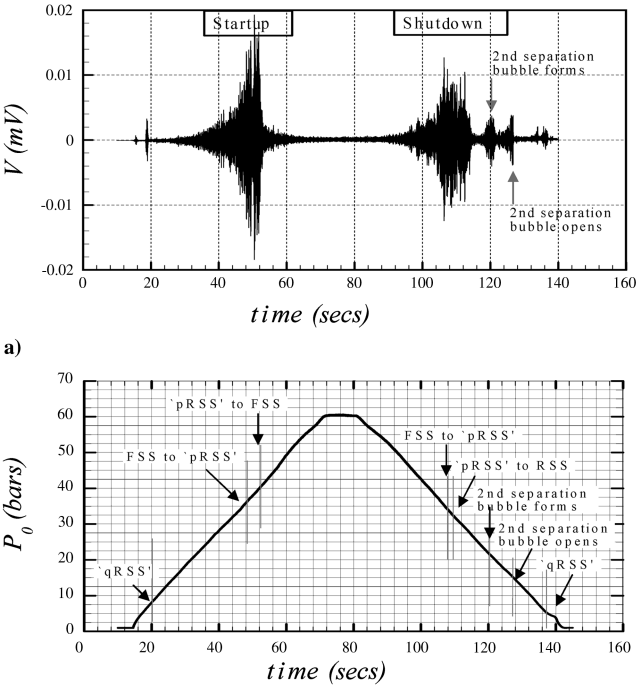

a)

b)

Fig. 12 Strain-gauge signal in *XY* direction from one of the test campaigns, showing the appearance of peaks (signifying the existence of lateral forces) during startup and shutdown phases.

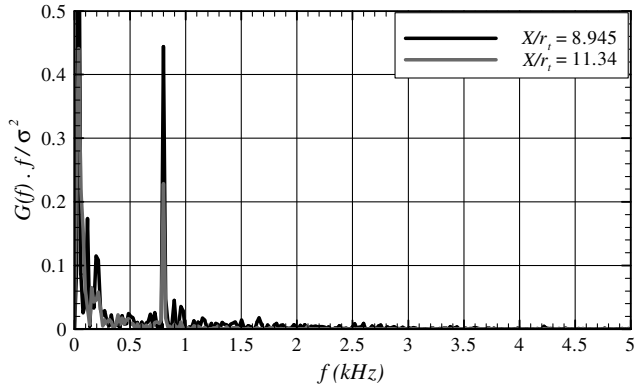

a) RSS

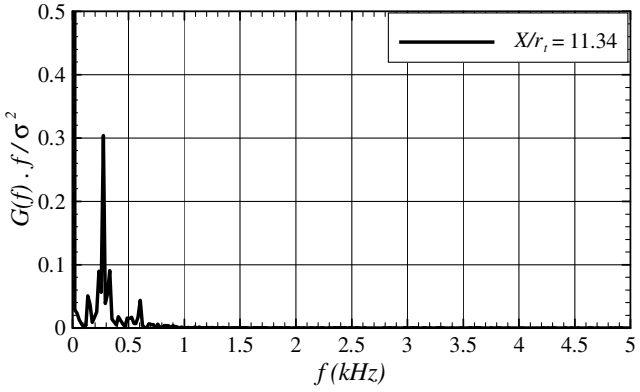

b)

Fig. 13 Spectral analysis of pressure signal a) from the ninth and 12th pressure points during RSS for NPR = 26 (the ninth point is in the separation bubble and the 12th point is in the reattachment region), and b) at the 12th pressure point during pRSS for NPR = 35.

Figure 10 helps explain the type of shock motions that can be extracted from the pressure signals shown in Fig. 9c. Flow is considered from left to right. Take the case of transducers 10 and 11 which show pressure signals with mirror imaging, as depicted by case II, Fig. 10b. Points A, B, C, and D are shown as the axial locations of transducers on the nozzle wall and SW indicates a shock wave. As the shocks oscillate, at some time instant t_1, SW1 is ahead of point B and SW2 is behind point D. At this time, point B will show higher wall pressure (being ahead of SW1) and point D lower. When SW1 moves behind point B, time t_2, it will show lower wall pressure, whereas, at the same instant, if SW2 moves ahead of point D, wall pressure from point D will show higher value. The opposite will occur when these shocks move to their original starting positions t_3. The type of signal that points B and D will generate under such an oscillatory motion will be a mirror image of each other, as shown in case II, Fig. 10b. Another type of shock motion that is observed is that captured by transducers located at positions 8 and 10 and 11 and 12. In this case, the pressure signals were observed to fluctuate up and down at the same instant, indicating that both SW1 and SW2 cross points B and D in same direction and at the same time. Case I, Fig. 10a, shows this signal behavior generated for this type of shock motion. Case II, Fig. 10b indicates that the combined movement of separation and reattachment shocks results in an expansion and contraction motion of the separation bubble, generally known as "breathing motion" [27], which in turn seems to be triggered, as suggested by Maull [28], by the imbalance of the mass of fluid reversed at the reattachment point to that scavenged from the separation point. On the other hand, the dynamic wall pressure behavior of the eighth pressure point elucidates that the separation shock undergoes large-scale streamwise oscillatory motion or "flapping" of the shock wave, case I, Fig. 10a.

Normally, after flow reattachment, the flow would continue to be attached to the nozzle wall up to the nozzle exit. However, Frey and Hagemann [1] suggested that, during RSS, if a strong shock hits the nozzle wall downstream of the first reattachment point, the flow might even be forced to separate from the wall for a second time. Later on, reattachment of this separated flow may cause a second separation bubble to form. Figure 11a shows the mean wall pressure distributions for a range of NPRs that experience the RSS condition during shutdown. Each of these distributions is obtained from independent test campaigns with the NPR held constant for 15 s, as shown in Fig. 4. It can be clearly discerned from these plots that, as the NPR is reduced below 22, a second peak in wall pressure (above P_a) begins to appear, indicating the formation of a second reattachment point close to the nozzle exit. In between the first and second pressure peaks, the wall pressure is seen to go below the ambient value forming a small plateau region. This indicates the presence of a second separation bubble. This flow phenomena is very clearly seen for NPR = 18 (Fig. 11a). The presence of a second separation bubble has also been reported by Stark et al. [14] (during shutdown) using infrared thermometry and Nguyen et al. [29,30] (during startup). At NPR = 16, however, this second pressure plateau is seen to disappear, suggesting opening of the second separation bubble. Figure 11b shows a hypothetical sketch of the

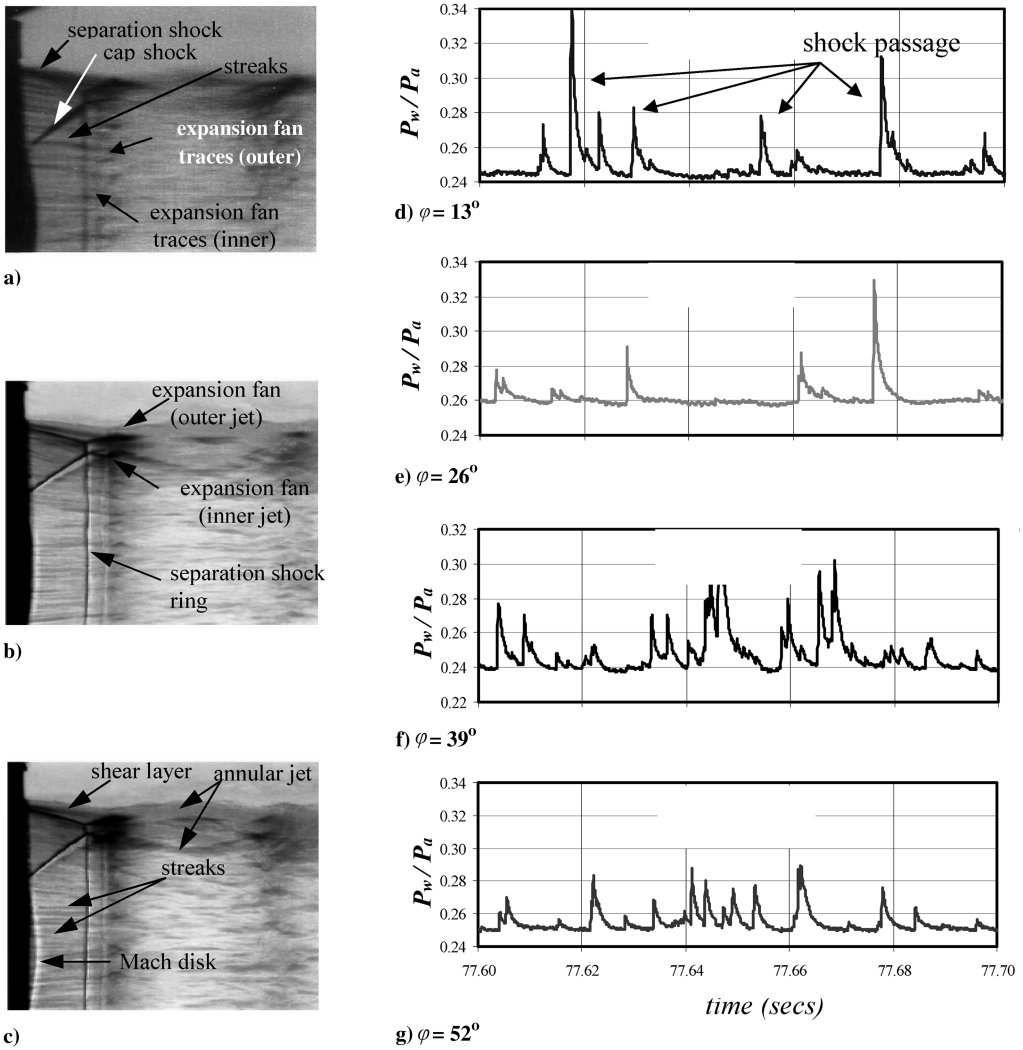

Fig. 14 Flow characteristics under rippling shock motion; schlieren pictures of the exhaust flow pattern for NPR = 52 with a) knife edge perpendicular to flow direction, and b–c) knife edge parallel to flow direction (pictures taken at two time instants); d–g) simultaneously sampled wall pressure signals at four circumferential positions (each 13 deg apart) at the 12th axial pressure location, NPR = 52.

RSS in the TOP nozzle along with the prevalent shock motions and the appearance of a second separation bubble. The extent of the second separation bubble is much smaller than the first one, which, in turn, is dictated by the complex reflection of shocks in the annular jet, as shown in Fig. 11b.

Figure 12a shows the strain-gauge signal for a particular test campaign with ramp up and ramp down rates of 1 bar/s. Each of the observed peaks signifies a particular flow transition and are marked in Fig. 12b. Earlier studies [3–8,13,19] have shown that flow transitions such as FSS $\rightarrow$ RSS (forming of separation bubble) and RSS $\rightarrow$ FSS (opening of separation bubble) result in strong peaks in the side-load signal. It can be seen that, during shutdown, very distinct peaks in the strain-gauge signal are observed at approximately NPR = 22 and then at NPR = 16. So in continuation of our discussion from the preceding paragraph, we conclude that the formation and opening of the second separation bubble also contributes to peaks in the strain-gauge signal, as shown in Fig. 12a. This is an important result, as the explanation to the origin of these peaks was not reported before and was thought of only as a consequence of the RSS condition.

Spectral Analysis

It is known that the power spectral density of the wall pressure signal helps to clearly show that the large-amplitude, high-energy fluctuations, those caused by shock motion, fall in a fairly narrow low-frequency band. Plotting $G(f).f/\sigma^2$ vs f on a linear–linear scale highlights the dominant frequency ranges in the signal. Figure 13a shows the power spectral density of the wall pressure fluctuations during RSS (NPR = 26, shutdown) for the ninth and 12th pressure point locations. These pressure points were specifically chosen because the sampling frequency of these was 10 kHz, whereas those of others were only 1 kHz. The main idea was to capture the frequency of oscillations prevalent in the separation bubble (ninth) and reattachment region (12th). Though these pressure points are not located at the exact separation or reattachment locations, once RSS occurs, the whole system of shocks will oscillate as a single unit. It can be clearly discerned from Fig. 13a that, under the RSS condition, the high-amplitude pressure fluctuations generated by the shock wave motion are distributed in the range of 220–1 kHz with a prominent peak at 800 Hz. The low-frequency peaks at 156 and 220 Hz could perhaps be due to the residual effect of both the large-amplitude fluctuations experienced due to movement of the separation bubble and those experienced due to flow in the backflow region downstream of the reattachment region, causing low-amplitude perturbations in the overall pressure fluctuations in the region of interaction. A similar analysis was made for the flow under the pRSS regime (Fig. 13b). The plot shows the pRSS regime dominated by a frequency centered around 250 Hz.

Rippling Shock Motion

Another type of shock motion that has been observed to exist in two-dimensional shock wave boundary-layer flows [27] is the spanwise "ripples" experienced by the shock plane, which adds three-dimensionality to the shock structure. Some effort was also made in the present study to see if rippling shock motion exists in nozzle flows. Figures 14a–14c show the schlieren pictures of the exhaust flow at NPR = 52. The picture in Fig. 14a is obtained with a knife edge perpendicular to the flow direction, whereas Figs. 14b and 14c are those with a knife edge parallel to the flow direction, respectively. The various observed flow features are marked on the pictures. One particular flow feature that is of interest here is the longitudinal streaks in the flow that end up at the origin of the expansion fans (outer jet) (Figs. 14a and 14b). Tests were specially planned to look into the origin of these streaks. Previous tests had shown the physical separation line to be a little downstream of the 12th pressure point for NPR = 52. This 12th axial pressure location also has four additional pressure transducers located circumferentially, each 13 deg apart and sampled at high frequency. So with the NPR held constant, three schlieren pictures were taken (xenon flash lamp with flash duration of 13 ms and flash energy of 18 J), each with a time interval of 1 s

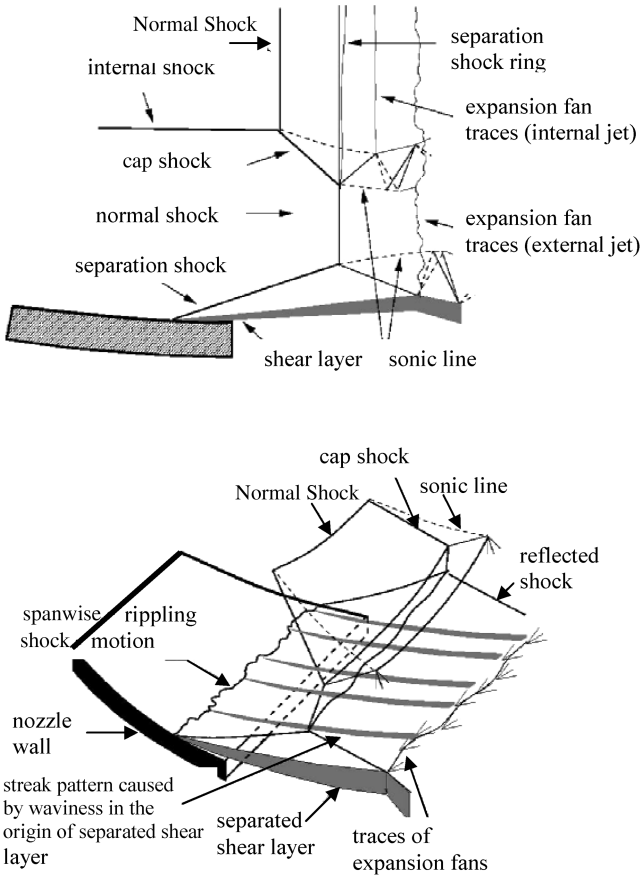

Fig. 15 Schematic sketch of the exhaust flow structure from a TOP nozzle as developed from color schlieren pictures, showing the prevalent rippling shock motion and its effect in the origin of observed flow details.

(Figs. 14b and 14c). Figure 14 reveals some important details. Firstly, the separation shock ring is not straight but shows some waviness. Secondly, the lateral position of streaks (seen as dark longitudinal lines in the flow) is seen to vary with time. Wall pressure signals from the four spanwise pressure point locations, Figs. 14d–14g, show that the shock passes (as seen by peaks in wall pressure) different spanwise pressure points at different time intervals. The origin of these streaks is due to the small density gradients created locally by the spanwise rippling shock motion. It is known that Goertler-type vortices are induced in the throat region, contributing to stratification through oil upstream of the separation point, as seen in Fig. 9a. The presence of these vortices may perhaps be responsible for triggering the observed rippling motion. Figure 15 shows a schematic view of the flow details (side view and isometric) as developed from the schlieren pictures and the origin of flow structure due to rippling shock motion at the separation location. This preceding study indicates that the separation shock not only translates back and forth (flapping) but also experiences large-scale spanwise perturbations (rippling).

Conclusions

An experimental study has been conducted to study the flowfield features prevalent during a pRSS condition, end-effect regime, and a fully formed RSS condition in a subscale thrust optimized parabolic nozzle. During a pRSS condition, the wall pressure signal randomly alternates between its value in the backflow region and that above ambient (FSS to RSS transition condition and vice versa) as a function of time. A surface oil study shows no region of oil accumulation downstream of the physical separation line, and the schlieren images of exhaust flow are seen to fluctuate significantly in its lateral extent; whereas, during a fully formed RSS condition, the wall pressure signals in the region of flow reattachment, as seen in Fig. 9f and 9g, show values above ambient pressure. A surface oil study

reveals prominent separation bubble formation (region of oil accumulation) and a region of reattachment. These flow characteristics suggest that the RSS condition therefore needs to be broadly subdivided into a partially formed RSS (occurs when the separation point approaches closer to the nozzle exit but before the end effect finally occurs) and a fully formed RSS.

During transient tests, surface oil-pigment pictures show upstream and downstream movement of the separation front during pRSS $\rightarrow$ FSS transition and vice versa during startup and shutdown sequences, respectively. However, the pRSS $\rightarrow$ FSS transition during shutdown is followed by a fully formed RSS condition unlike the case during startup, suggesting a change in the relative axial positions of normal and overexpansion shocks at similar nozzle pressure ratios. Under an RSS condition during shutdown, the presence of a second separation bubble is identified and it is found that the formation and opening of this bubble also contributes to peaks in the strain-gauge signal.

The time history of wall pressure signals from adjacent pressure transducers during the RSS condition indicate the existence of a large-scale flapping motion of the separation shock, whereas another type of shock motion is observed across the separation bubble in which the separation and reattachment shocks move in opposite directions generating pressure signals that are mirror images of each other. The latter movement suggests that the separation bubble breathes during its lifetime wherein it exhibits a low-frequency expansion and contraction motion. This motion can contribute toward an increase in overall flow unsteadiness during the RSS condition. In addition to the preceding shock movements, the overexpansion shock also experiences spanwise perturbations (rippling motion).

Acknowledgments

The results reported in this paper are from the work carried out by the first author during his tenure as a research scientist in the Nozzle Flow Group at Space Propulsion Institute, DLR, German Aerospace Center, Lampoldshausen, Germany between May 2001 and December 2003. The authors would like to thank Ralf Stark and H. K. Ciezki for the useful discussions and Herr Kroenmueller and Christian Boehm for their immense help during the entire course of the experiments.

References

[1] Frey, M., and Hagemann, G., "Status of Flow Separation Prediction in Rocket Nozzles," AIAA Paper 98-3619, 1998.

[2] Frey, M., "Shock Patterns in the Exhaust Plume of Rocket Nozzles," *Proceedings of the 3rd European Symposium on Aerothermodynamics of Space Vehicles*, ESA, SP-426, 1998, pp. 395–403.

[3] Frey, M., and Hagemann, G., "Restricted Shock Separation in Rocket Nozzles," *Journal of Propulsion and Power*, Vol. 16, No. 3, 2000, pp. 478–484. doi:10.2514/2.5593

[4] Hagemann, G., Frey, M., and Koeschel, W., "Appearance of Restricted Shock Separation in Rocket Nozzles," *Journal of Propulsion and Power*, Vol. 18, No. 3, 2002, pp. 577–584. doi:10.2514/2.5971

[5] Oestlund, J., Damgaard, T., and Frey, M., "Side-Load Phenomena in Highly Overexpanded Rocket Nozzles," *Journal of Propulsion and Power*, Vol. 20, No. 4, 2004, pp. 695–704. doi:10.2514/1.3059

[6] Frey, M., and Hagemann, G., "Flow Separation and Side Loads in Rocket Nozzles," AIAA Paper 99-2815, 1999.

[7] Frey, M., "Behandlung von Stroemungsproblemen in Raketduesen bei Ueberexpansion," Ph.D Thesis, Inst. fuer Aerodynamik and Gasdynamik, Univ. of Stuttgart, Germany, 2000.

[8] Frey, M., Stark, R., Ciezki, H. K., Quessard, F., and Kwan, W., "Subscale Nozzle Testing at the P6.2 Test Stand," AIAA Paper 2000-3777, 2000.

[9] Terhardt, M., Hagemann, G., and Frey, M., "Flow Separation and Side-Load Behavior in the Vulcain Engine," AIAA Paper 99-2762, 1999.

[10] Watanabe, Y., Sakazume, N., and Tsuboi, M., "LE-7A Engine Nozzle Problems During the Transient Operations," AIAA Paper 2002-3841, 2002.

[11] Watanabe, Y., Sakazume, N., and Tsuboi, M., "LE-7A Engine Separation Phenomenon Differences of the Two Nozzle Configurations," AIAA Paper 2003-4763, 2003.

[12] Nave, L. H., and Coffey, G. A., "Sea Level Side Loads in High-Area-Ratio Rocket Engines," AIAA Paper 73-1284, 1973.

[13] Hoegman, U., Mattsson, J., and Torngren, L., "A Sub-Scale Test Programme on Investigation of Flow Separation and Side-Loads in Rocket Nozzles," *Proceedings of the 3rd European Symposium on Aerothermodynamics of Space Vehicles*, ESA, SP-426, 1998, pp. 373–378.

[14] Stark, R., Kwan, W., Quessard, F., Hagemann, G., and Terhardt, M., "Rocket Nozzle Cold-Gas Test Campaigns for Plume Investigations," *4th European Symposium on Aerothermodynamics for Space Vehicles*, ESA, SP-487, Dec. 2001, pp. 611–618.

[15] Kwan, W., and Stark, R., "Flow Separation Phenomena in Subscale Rocket Nozzles," AIAA Paper 2002-4229, 2002.

[16] Gross, A., and Wieland, C., "Numerical Simulation of Separated Cold Gas Nozzle Flows," *Journal of Propulsion and Power*, Vol. 20, No. 3, 2004, pp. 509–519. doi:10.2514/1.2714

[17] Hagemann, G., Kruelle, G., and Hannemann, K., "Numerical Flowfield Analysis of the Next Generation Vulcain Nozzle," *Journal of Propulsion and Power*, Vol. 12, No. 4, 1996, pp. 655–661. doi:10.2514/3.24086

[18] Verma, S. B., and Ciezki, H. K., "Unsteady Nature of Flow Separation Inside a Thrust Optimized Parabolic Nozzle," AIAA Paper 2003-1139, 2003.

[19] Verma, S. B., Stark, R., and Haidn, O., "Relation Between Shock Unsteadiness and the Origin of Side-Loads in a Thrust Optimized Parabolic Rocket Nozzle," *Aerospace Science and Technology*, Vol. 10, No. 6, Aug. 2006, pp. 474–483. doi:10.1016/j.ast.2006.06.004

[20] Verma, S. B., "Study of Flow Separation in Truncated Ideal Contour Nozzle," *Journal of Propulsion and Power*, Vol. 18, No. 5, 2002, pp. 1112–1121. doi:10.2514/2.6042

[21] Gross, A., Haidn, O., Stark, R., Zeiss, W., Weber, C., and Weiland, C., "Experimental and Numerical Investigation of Heat Loads in Separated Nozzle Flow," AIAA Paper 2001-3682, 2001.

[22] Verma, S. B., and Haidn, O., "Goertler Vortex Formation During the Shut Down Sequence Inside a Thrust Optimized Parabolic (TOP) Rocket Nozzle," AIAA Paper 2005-518, 2005.

[23] Wong, H. Y. W., "Overview of Flow Oscillations in Transonic and Supersonic Nozzles," *Journal of Propulsion and Power*, Vol. 22, No. 4, 2006, pp. 705–720. doi:10.2514/1.12723

[24] Manski, D., and Hagemann, G., "Influence of Rocket Design Parameters on Engine Nozzle Efficiencies," *Journal of Propulsion and Power*, Vol. 12, No. 1, 1996, pp. 41–47. doi:10.2514/3.23988

[25] Rao, G. V. R., "Exhaust Nozzle Contour of Optimum Thrust," *Jet Propulsion*, Vol. 28, No. 6, June 1958, pp. 377–382.

[26] Kistler, A. L., "Fluctuating Wall Pressure Under a Separated Supersonic Flow," *Journal of the Acoustical Society of America*, Vol. 36, No. 3, 1964, pp. 543–550. doi:10.1121/1.1918998

[27] Dolling, D. S., and Narlo, N. C., II., "Driving Mechanism of Unsteady Separation Shock Motion in Hypersonic Interactive Flow," *Aerodynamics of Hypersonic Lifting Vehicles*, AGARD CP-428, 1987, pp. 7.1–7.12.

[28] Maull, D. J., "Hypersonic Flow over Axially Symmetric Spiked Bodies," *Journal of Fluid Mechanics*, Vol. 8, No. 4, 1960, pp. 584–592. doi:10.1017/S0022112060000815

[29] Nguyen, A. T., Deniau, H., Girard, S., and Alizary de Roquefort, T., "Wall Pressure Fluctuations in an Overexpanded Rocket Nozzle," AIAA Paper 2002-4001, 2002.

[30] Nguyen, A. T., Deniau, H., Girard, S., and Alizary de Roquefort, T., "Unsteadiness of Flow Separation and End-Effects Regime in a Thrust-Optimized Contour Rocket Nozzle," *Flow, Turbulence and Combustion*, Vol. 71, Nos. 1–4, 2003, pp. 161–181. doi:10.1023/B:APPL.0000014927.61427.ad

D. Talley
Associate Editor